INTENSITY CONTROL OF DIELECTRIC BARRIER DISCHARGE FILAMENTS

by

MATTHEW CRAWFORD PALIWODA

A THESIS

Presented to the Faculty of the Graduate School of the

MISSOURI UNIVERSITY OF SCIENCE AND TECHNOLOGY

In Partial Fulfillment of the Requirements for the Degree

MASTER OF SCIENCE IN AEROSPACE ENGINEERING

2016

Approved by

Joshua L. Rovey Ph.D., Advisor
Xiaodong Yang, Ph.D
Carlos H. Castano, Ph.D

ABSTRACT

When operated in a filamentary mode, a volume dielectric barrier discharge (DBD) is known to produce patterned plasma structures. These structures are currently being explored for reconfigurable metamaterial applications. In this work the presence and intensity of a single filament, within an array of filaments, was controlled by adjusting the voltage to that filament's individual needle electrode. The current, voltage, and time-averaged normalized light intensity were measured while varying the voltage of the needle through a self-biasing resistance. For a 7.5 kV, 3.2 kHz DBD in air, the needle-controlled filament intensity varies from that of the surrounding filaments to zero measurable light intensity. The total bias on the needle does not exceed 7 % of the driving voltage. Analysis of an electrostatic field model showed that the varying intensity filament does not produce light when the curve of the electric field along the filament centerline is below the curve of the electric field along the centerline of an adjacent unbiased filament. Surface charge interaction, on the dielectric barrier furthest from the needle electrode, is the mechanism that extinguishes the filament while the applied electric field is above the dielectric strength of air. The light intensity was calculated as the total charge transferred across the filament. The total charge was estimated from the simulation model and varies with the measured light intensity.

ACKNOWLEDGMENTS

I am extremely grateful to my advisor, Dr. Joshua Rovey, for the opportunity, support and guidance over the past two years. The laboratory independence and freedom to pursue different avenues of thought made the research experience an absolute pleasure.

I would like to thank both Dr. Rovey and the Aerospace and Mechanical Department at Missouri S&T for the graduate research assistant positions and the graduate teaching position that provided financial support for this degree.

I would like to thank my committee members Dr. Carlos Castano and Dr. Xiaodong Yang for their assistance and insight.

I would like to thank my fellow students and friends for their technical and moral support: Dr. Warner Meeks for his mentorship in the laboratory, Mitch Wainwright for his computer simulation work on this project, and Joshua Heck for assistance finishing the thesis.

Finally, I would like to thank my family and friends for their advice, support, and proof reading. To my parents, thank you for everything.

TABLE OF CONTENTS

LIST OF ILLUSTRATIONS

Page

NOMENCLATURE

Symbol	Description
A	Surface Area
B	Magnetic Field
B_{avg}	Average Magnetic Field
D	Displacement Field
D_{avg}	Average Displacement Field
E	Electric Field
E_{avg}	Average Electric Field
E_o	Baseline Electric Field
E_r	Electric Field of Electron Avalanche
H	Magnetic Strength
H_{avg}	Average Magnetic Strength
$G_{\|\|}$	Translation Vector
J_e	Electron Current Density
J_1	Bessel Function
L	Path Length
R	Filament Radius
S	Integral Surface
V	Voltage
a	Lattice Constant
e	Elementary Charge
m_e	Electron Mass
n	Surface Normal Unit Vector
n_e	Electron Number Density
n_g	Neutral Gas Number Density
n_{ineg}	Negative-Ion number Density
n_{ipos}	Positive-Ion Number Density
p	Pressure
q	Surface Charge

r	Surface Charge Area Radius
t	Time
t_o	Streamer Initiation Time
u_e	Electron Drift Velocity
x	Position Parallel to Dielectric Surface
z	Position Across the Air Gap
α	First Townsend Coefficient
ε_{eff}	Effective Permittivity
ε_o	Permittivity of Free Space
$\overline{\varepsilon}$	Permittivity in Fourier space
κ	Inverse Fourier Coefficient
μ_{eff}	Effective Permeability
ρ	Volume Charge Density
ν_c	Electron-Neutral Collision Frequency
σ	Surface Charge Density
σ_{en}	Electron-Neutral Collisional Cross-Section
ϕ	Electric Potential
ψ	Light Intensity Flux Rate
$\overline{\psi}$	Time-Space Integrated Light Intensity
ω	Incident Electromagnetic Wave Frequency
ω_{pe}	Plasma Electron Frequency

1. INTRODUCTION

Filamentary plasma has been previously studied for application in the growing field of microwave metamaterials due to its electrically variable structure, variable negative permittivity, and sub-microwave scale. [1-9] Metamaterials are artificial periodic composite structures that create permittivities and permiabilities not commonly found in nature, including negative values. Manipulation of these two material properties leads to unique propagation of electromagnetic waves through the material, such as negative refraction. Metamaterials have application in communication, radar, signal processing, energy transfer, and non-destructive sensing.

1.1. METAMATERIALS

A metamaterial modifies electromagnetic wave propagation by resonating with the wave fields on a subwavelength scale, inducing opposing electromagnetic fields and shifting the average displacement field/magnetic field away from the average electric field/magnetic field strength, as expressed in Equation 1. Pendry et al. initially discussed filling space with thin wire resonators to allow wave propagation bellow the plasma cut-off frequency of the wire[10] as well as the relocation of electromagnetic energy to modify the permeability and permittivity of split ring resonators.[11]

$$\varepsilon_{eff} = \frac{D_{avg}}{\varepsilon_o E_{avg}} \tag{1a}$$

$$\mu_{eff} = \frac{B_{avg}}{\mu_o H_{avg}} \tag{1b}$$

For a metal wire hexagonal lattice structure, the relation between the geometric arrangement of the wires – defined by the wire radius (R) and the separation between wires or lattice constant (a), – and the material properties of the metal wires – defined by the electron frequency (ω_{pe}) and the permittivity of the surrounding gas (ε_g), – determines the effective perimittivity (ε) of the composite material, as expressed in

Equation 2 and Equation 3.[12] The permittivity is expressed in its inverse Fourier coefficients (κ) in Equation 4, whereby $(x_\parallel)$ is the position vector of the lattice structure, (ω) is the frequency of the incident electromagnetic wave, and $(G_\parallel)$ is the translation vector, a function of the reciprocal lattice. Numerical methods are used to define more complex structures that do not have an analytical solution.

$$\varepsilon(x_\parallel \mid \omega) = \sum_{G_\parallel} \bar{\varepsilon}(G_\parallel) e^{jG_\parallel x_\parallel} \tag{2}$$

$$\kappa(G_\parallel) = \left(\frac{\omega^2 + j\nu_c\omega}{\omega^2 + j\nu_c\omega - \omega_{pe}^2} \right) \frac{2\pi R^2}{a^2 3\sqrt{3}} + \frac{1}{\varepsilon_g}\left(1 - \frac{2\pi R^2}{a^2 3\sqrt{3}}\right), \qquad G_\parallel = 0 \tag{3}$$

$$\kappa(G_\parallel) = \left(\left(\frac{\omega^2 + j\nu_c\omega}{\omega^2 + j\nu_c\omega - \omega_{pe}^2} \right) - \frac{1}{\varepsilon_g} \right) \frac{2\pi R^2}{a^2 3\sqrt{3}} \frac{2J_1(G_\parallel, R)}{(G_\parallel, R)}, \qquad G_\parallel \neq 0 \tag{4}$$

1.2. PLASMA AS METAMATERIAL

Plasma's non-linear permittivity makes it a prime candidate for metamaterial application. The complex plasma permittivity is defined by Equation 5,[13] dependent upon the incident wave frequency (ω), the electron plasma frequency (ω_{pe}), and the collisional frequency (ν_c). By adjusting the plasma frequency, the permittivity can be tuned between unity and negative values of permittivity for a given incident wave frequency.

$$\varepsilon_{eff} = \left(1 - \frac{\omega_{pe}^2}{\omega^2 + \nu_c^{\,2}}\right) - j\left(\frac{\omega_{pe}\nu_c / \omega}{\omega^2 + \nu_c^2}\right) \tag{5}$$

Structures providing negative permeabilities, such as ring resonators and helix structures,[14] immersed in plasma have been investigated for creating a negative index of refraction metamaterial. In these structures, plasma is the component that provides the negative permittivity. Another benefit of plasma is that it provides electrical variability,

since the electron frequency is related to the plasma density (n_e) by Equation 6[13] and varies with the applied voltage and frequency.[9, 15] By tuning the plasma's electron density, a desired permittivity can be obtained during operation. This creates a variable index of refraction, or range of frequencies, over which the metamaterial can function.

$$\omega_{pe} = \sqrt{\frac{n_e e^2}{\varepsilon_o m_e}} \tag{6}$$

Another aspect of the plasma is its physical malleability, forming plasma as a periodic structure instead of as a homogeneous material. The permittivity can be further altered by changing the lattice constant of the structure. Then the permittivity is then dependent upon the plasma structure in addition to the electron density and collisional frequency. Thus, by varying the structure, the bandwidth for a given permittivity is extended.

A large variety of solid variable metamaterials in the microwave frequency have been investigated.[16] However, variability of these structures is limited by their electrical and structural components. The demonstrated bandwidth is on the order of ~5GHz. Plasma metamaterial variability is limited only by the electron density and the bounds that define its physical structure, providing a potentially larger bandwidth.

In addition to being tunable, the plasma can sustain high energy waves without failure due to its inherent high energy state. High power microwaves (HPM), defined by Benford and Swegle[17] as frequencies between 1 and 300GHz and peak power levels above 100 MW, are a potential niche area for plasma metamaterial application. Solid metamaterials have been investigated for HPM; however, gas breakdown,[18] material combustion,[19] and losses from failed components[20] due to large electric fields between components of a centimeter scale have proven to be an issue. For plasma based metamaterials, gas breakdown defines the microstructure, which eliminates ionization as a design limitation. Application of high energy microwaves includes directed energy weapons, plasma heating, radar, communication systems, and high energy particle research.[17, 21, 22]

1.3. DBD AS A RECONFIGURABLE METAMATERIAL

Filamentary dielectric barrier discharge (DBD) as a potential metamaterial is of particular interest due to its inherent microstructure. A DBD plasma filament is formed by discharging gas between two parallel plates that are covered with dielectric material, producing filaments (plasma columns ~0.1 mm in diameter) across the gas gap.[23, 24] The filaments have surface charges on the dielectric and space charges in the gas gap which interact with one another.[25] These dynamics limit the number of neighboring filaments; creating a memory effect that promotes filament restrike at the same location during the reversed polarity of the AC voltage.[25, 26] These filaments and their dynamics provide the structural element and mechanism to define a two dimensional microstructure made of plasma columns, similar to the thin rod metamaterials.

The filaments' interaction with an incident electromagnetic wave is defined by their permittivity. They support electric fields parallel with the plasma columns (transverse electric waves – TE waves), similar to wire photonic crystals, as well as plasmons that travel around the column surfaces created by the interface between the negative and positive permittivities (transverse magnetic waves – TM waves).[27]

Research using plasma filaments to construct metamaterials and affect the propagation of electromagnetic waves has focused on plasma photonic crystals (PPC) for application to microwaves.[9] Sakai et al[7] used individual cathode electrodes without a dielectric surface to demonstrate that bandgaps occur in plasma filament photonic crystals.[6] In addition to the plasma potential for bandgap waveguides, Sakai et al [7] demonstrated a waveguide consisting of a single row of filaments transmitting a signal around a ninety degree turn. Dong et al[2-4] has focused on demonstrating the formation of plasma structures in self-organized DBDs, and then numerically modeling the resulting bandgaps. Zhang et al,[28-30] conducted numerical models on exotic two dimensional plasma structures, exploring more diverse band structures than those previously demonstrated in self-organized DBDs. Methods for solving arbitrary geometries numerically for band gaps have been developed so that more elaborate geometric structures may be analyzed.[29, 30] For these geometries, direct control of the plasma position would be necessary to physically recreate their effect.

Plasma filaments are similar to the thin metal rods in previously demonstrated metamaterials since both permittivities are described by the Drude model, Equation 5. Although metal rods serve best to excite changes in the permittivity when resonating with TE waves, Park and Wu[31] demonstrated a negative permeability excited by TM waves using square clusters of metal rods. The clusters enhanced the magnetic dipoles created by the electric field traveling around the cluster, perpendicular to the filament axis. Further, they numerically calculated a negative index of refraction with the composite of negative permeability wire clusters and negative permittivity metal components.[32] Plasma's capability for negative permittivity and the potential to create a negative permeability through filament clusters suggests a similar plasma composite could produce negative index of refraction.

1.4. FOCUS OF CURRENT WORK

Control of the filament structural position has been demonstrated using both fixed electrode arrays[6-8] and self-organized DBDs.[1-5] The self-organized filament DBDs form organized structures over the entire surface of a DBD due to limiting interactions between filaments. However these organized structures link structure, filament size, and electron densities to the two independent variables of driving frequency and applied voltage. They are also limited to a maximum lattice dimension on the order of the filament's surface charge and there is no direct method for implementing predesigned and simulated structures.

Fixed individual electrode filaments allow for direct position control of the filaments but limit the variety of structural arrangements in the PPC to the grid assembly of the individual electrodes. Those demonstrating individual control over each electrode require a kilovolt switching or separate driving mechanism. Self-organizing DBD structures using arrays of individual electrodes have been demonstrated[3, 8] and show that filament discharges can occur in between electrode surface positions, extending the bandwidth of the system; however, for these demonstrations, each electrode was driven by the same voltage.

The eventual goal of the presented work is to form electrode arrays behind a dielectric individually controlling the filaments over the entire surface of the dielectric. The application could then be extended to discharging filaments between the electrode surface positions and manipulating the filaments with the surrounding electrode potentials. Since the total average voltage can be increased while maintaining relative voltage differences between individual electrodes, the electron density and position become uncoupled. By using voltage to control the filament position, the structural tuning remains electrical. The position and electron density of each filament is then independently controlled with electrical signals over the entire surface of the dielectric. With this approach, a larger range of effective permittivities may be directly implemented during DBD operation.

1.5. PARAMETERS OF DBD PLASMA

The applied conditions for a DBD plasma, such as gas pressure, gas species, voltage, and frequency determine the two defining parameters of a plasma microstructure element: the permittivity and the filament's radius. DBD filaments have electron densities of 10^{13}-10^{15} (cm^{-3}).[33] At atmospheric pressure in air the neutral gas density is 2.5 x 10^{19} kg/cm^3. This makes the degree of ionization < 10^{-3} %, defining the gas as weakly ionized, where the main form of collision is with neutrals. The collision frequency is then dependent upon the pressure and molecular make up of the gas. For the presented results, atmospheric air was used, defining a collision frequency of 260 GHz and estimated using Equation 7.[34] The collision frequency (ν_c) is equal to the product of the neutral gas number density (n_g), the electron-neutral collisional cross-section (σ_{en}),[35] and the drift velocity (υ_e).[36] The parameters are dependent upon the electron temperature (T_e), which can range from 1-10eV[33] but is 3-4eV[37] for the presented experimental condition. The electron temperature does not change with pressure, and is weakly proportional to the driving voltage.[15]

$$\nu_c = n_g \sigma_{en} u_e \tag{7}$$

The cut-off electron frequency, calculated using Equation 6, under which an incident wave will experience a negative permittivity, is 30GHz to 300GHz. These frequencies produce wavelengths in the microwave range of 10mm to 1mm. With a defined pressure and gas species, the electron density is determined by the applied DBD voltage and frequency.[15] The filament diameter is a lower dimensional bound to the applicable incident wavelength. For a fixed pressure, the radius of the filament depends upon the driving voltage[38] and frequency.[39]

1.6. STREAMER DISCHARGE THEORY

The type of discharge that forms DBD plasma columns is a streamer discharge. The theory was initially developed by Meeks, Loeb, and Raether[40, 41] to describe the disagreement between Townsend discharge and the observed discharge which precedes an arc. The streamer initiates with a Townsend discharge where an electron avalanche travels across the gas gap towards the anode. The difference between ion and electron drift velocities forms a concentration of electrons at the avalanche head and a trail of relatively stationary ions, creating a strong local electric field distortion at the head that opposes the applied electric field. The radius of the avalanche head grows due to diffusion and defines the field at the head. When the avalanche grows large enough for the distorted field to equal the applied field, electrons near the head experience a total force towards the head causing an intense multiplication of ionizations. Increased photons produced by ionization at the avalanche head increase secondary photoionization. The secondary electrons ahead and behind the streamer create a conductive path for the streamer to travel. The streamer then grows at the faster rate of the traveling photoionization process across the gap rather than the electron drift velocity.

Two types of streamers can form: either a positive or a negative streamer. They are directed in the positive or negative electric field direction. Photoionization leads the positive streamer towards the cathode along the distorted tail of the electron avalanche, extending the streamer with successive ionizations and directing the electrons through the conductive path of the streamer. Photoionization for a negative streamer leads the streamer towards the anode by creating sequential avalanches ahead of the initial

avalanche tip that provide a conductive path of ions for streamers electrons to travel along. Positive streamers are more often observed than the negative streamers and produce lower electron densities.[42]

After the streamer reaches both dielectric surfaces, the streamer acts as a highly conductive path for charge to transfer across. Surface charge builds up on the dielectric and distributes radially from the streamer. Built-up charge eventually shields the streamer from the applied electric field until the field driving the ionization process drops below the dielectric strength of air. At this point, the streamer is extinguished. Residual space and surface charge increases the electric field at the location of the streamer during the reversed polarity of the applied electric field so that another streamer discharges at the same location. The surface charge and space charge create a memory effect that causes the time-averaged light from multiple filaments to maintain its position.

2. EXPERIMENTAL SETUP

2.1. VOLUME DBD PHYSICAL AND ELECTRICAL SETUP

The DBD investigated in this work consists of two parallel copper mesh electrodes, both covered with microscope slide glass. The driving signal mesh electrode allows for end-on photos of the filament position across the surface of the dielectric. The mesh and dielectric barrier of the driving electrode are of dimensions that create a uniform charge distribution over the discharging surface: 0.15 mm opening (#100 mesh size), 0.056 mm wire diameter, and 1.0 mm thick dielectric.[43, 44] The grounded mesh electrode has an opening of 0.85mm (#20 mesh size), a 0.40 mm diameter wire, and a dielectric barrier thickness of 0.12 mm. The larger mesh size and thinner dielectric barrier are sufficient to create an electric field on the surface of the grounded dielectric barrier that causes filaments to preferentially discharge at the mesh nodes. The wire weave of the mesh used for the grounded electrode has an offset between the vertical and horizontal directions that keeps the vertical weave 0.12 mm away from the glass. The peak to peak sinusoidal amplitude of the horizontal wire weave is 0.92 mm and the vertical wire weave is 0.68 mm.

The DBD is mounted on an ABS plastic stand with acme screws on the side to permit fine tuning of the gap width. The air gap between the two plates is set at 1.0 mm. The mesh electrodes and dielectric cover a 22 mm by 22 mm area. Adhesive gel on the edge of the mesh prevents charge from making a direct path to the electrodes and thus ensures the current travels through the dielectric. A photograph of the DBD is shown in Figure 2.1. The DBD is operated at 6.5 kV, 7.5 kV, and 9.0 kV at 3.2 kHz.

A Canon EOS Rebel XL records the time-averaged discharge of the filament position and light intensity at an exposure time of 125 seconds. As shown in the electrical schematic of Figure 2.2, the driving voltage signal is created by a Rigol DG-1022 Function Generator, the power is supplied by a Crown Macro-Tech 1202 Audio Amplifier, and a Corona Magnetics 5525-2 Transformer with a turn ratio of 1:357 increases the voltage signal producing a maximum voltage of 25 kV with a frequency range of 0.9 – 5 kHz. A North Star PVM-5 High Voltage Probe, with a 1:1000 ratio, monitors the voltage supplied to the DBD. A 1:1 Pearson Current Probe, Model 114,

monitors the current through the system. A 1:10 Tektronix P2221 passive voltage probe reads the voltage across a 200kohm resistor in series with the larger resistor controlling the voltage at the positioned needle. Both the Pearson and the North Star Probes are recorded by an Agilent Infinium 500MHz 1GSa/s Model #54815A Oscilloscope.

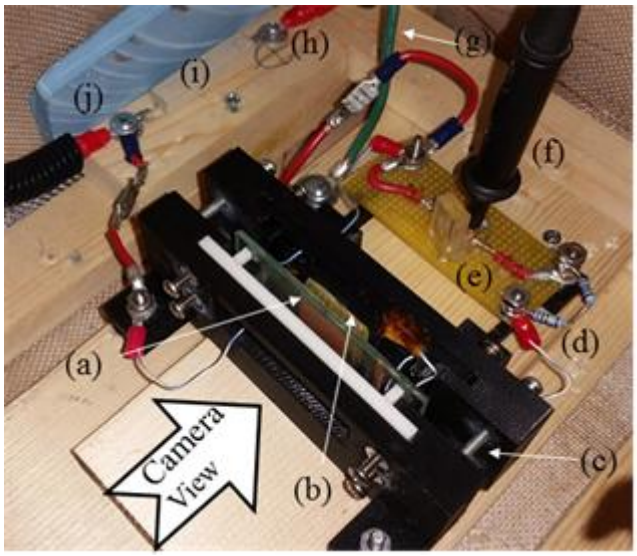

Figure 2.1. Photograph of DBD setup. The DBD consists of two parallel glass plates backed with (a) powered electrode and (b) grounded electrode. The air gap is controlled by (c) acme screws. Voltage across the (d) biasing resistors is measured using a voltage divider with (e) a 200kΩ reference resistor and (f) 10:1 voltage probe. Both grounded electrode and the voltage divider are referenced to (g) ground. Current supplied from the (h) transformer is limited by (i) a 5.9kΩ resistor to protect the transformer. The lead from the (j) high voltage probe measures voltage across the DBD.

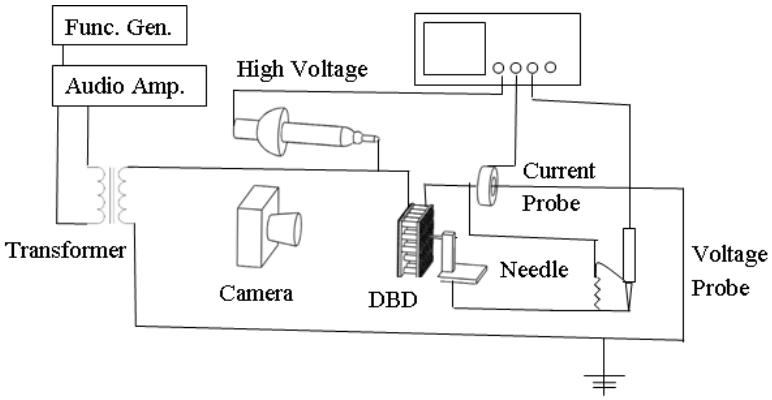

Figure 2.2. Diagram of experimental set up.

2.2. NEEDLE ELECTRODE SETUP

An independently electrically controlled needle is used to control the intensity of a plasma filament within the DBD. The needle and its electrical setup are shown in Figure 2.1 and Figure 2.2. The needle is constructed from a magnetic wire with flattened tip mounted flush to the back surface of the grounded dielectric barrier. The wire (diameter 0.57 mm) with an added Kapton insulation layer (0.14 mm thickness, $\varepsilon = 3.5$) is centered between the mesh so that the only electrical connections between the two are through the dielectric or their respective lead wires. Resistors connect the needle to ground causing the needle to have a non-zero floating potential or self-biasing potential. By adjusting the resistance, the self-biasing potential of the needle can be adjusted.

3. EXPERIMENTAL RESULTS

The following section presents the results from needle-controlled filament tests in the DBD. In some cases the DBD has 1mm gas gap, the voltage is set at 6.5 kV or 7.5 kV. When the driving voltage is at 9.0 kV, the air gap is at 1.5mm. Results are shown below for different DBD voltages, needle electrode self-biasing resistances, surface cleansings, and mesh self-biasing resistances.

3.1. FILAMENT PHOTOGRAPHS

Photographs of the DBD filaments for different self-biasing needle resistances are shown in Figure 3.1. This data is for the 6.5 kV DBD driving voltage. The regular pattern of dots is made up of individual DBD plasma filaments. The filaments form at alternating nodes over the grounded wire mesh electrode since the meshes' vertical wires are slightly below the mesh surface plane and cannot make a connection. For resistances below 4.7 MΩ, a filament clearly forms in between the wire mesh nodes at the needle location. As the needle's self-biasing resistance increases the filament light intensity decreases. It is clear from these photographs that the independent needle can control both the presence and intensity of the new filament. Resistance below 200 kΩ was investigated with a 1 kΩ resistor, however, prominent current spikes reduced the reliability of the measurement. Resistances above 30 MΩ were not investigated because the data showed further increases had no effect on the discharge of the filament.

To get a better measure of the intensity change at the needle-controlled filament, a photographic analysis was conducted. The numerical value of the photograph pixels at the needle-controlled filament location were compared with the pixel values for mesh filament and for a region with no filament (i.e., the mid-point between two mesh filaments). An 8x8 pixel square section of the photograph, fitting the size of the filament, was selected using Photoshop software and the average luminosity value of the area was used as the intensity value. A 15x15 size square section was used to select the average value of a region without any discharge and was subtracted from the intensity values. In this way the intensity of the needle-controlled filament was compared with a mesh

filament and also a region where there was no discharge. Figure 3.2 (b) shows the results as the ratio of the needle filament to the mesh filament and Figure 3.2 (a) shows the ratio of the needle filament to the background intensity for 6.5kV, 7.5kV, and 9.0kV. The error bars were created by taking the standard deviation of ten mesh node filaments between photos, averaging that deviation, and creating its ratio with the respective plot intensity.

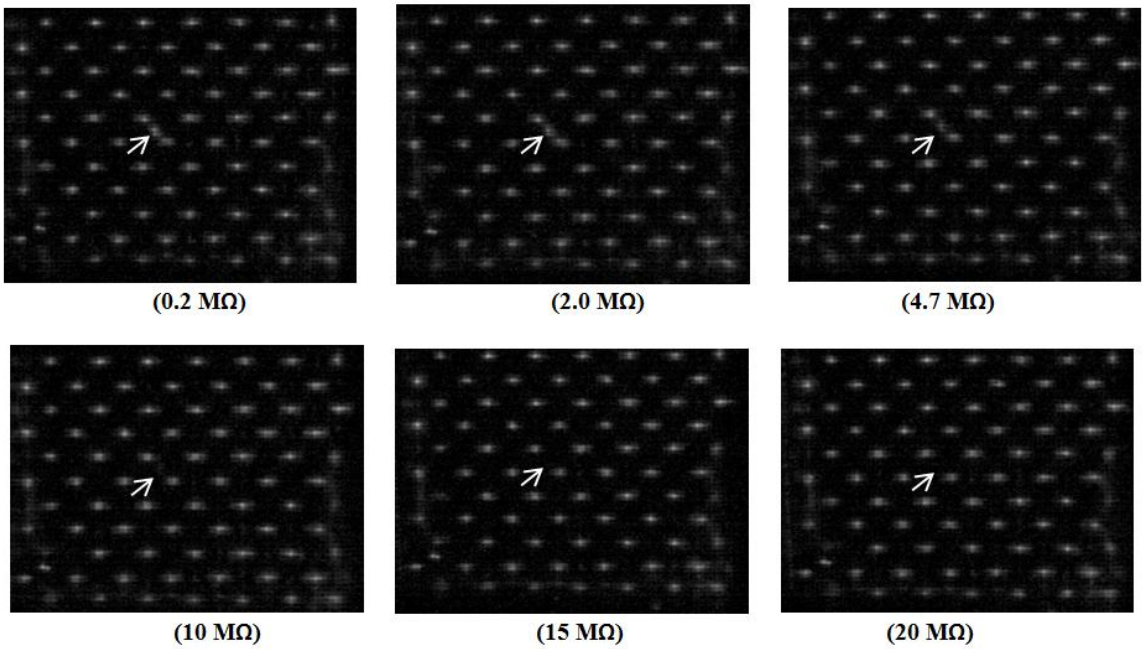

Figure 3.1. Photographs of the filament at the needle: on and off. End on view of the dielectric surface operating at 6.5 kV between the needle and ground reference. The arrow indicates the needle position.

The needle-controlled filament has a distinct on and off state. For resistances below 15 MΩ the ratio of the needle-filament to the mid-point goes to zero, signifying that the light intensity is the same as a non-discharging region. As the resistance decreases, the needle-filament turns on and becomes more intense. At the lowest resistance tested, 1kΩ, the needle-filament has an intensity that remains at 80% the intensity of the mesh nodes and 6 to 8 times brighter than the background region where no filaments are present for 6.5kV, 7.5kV, and 9.0kV.

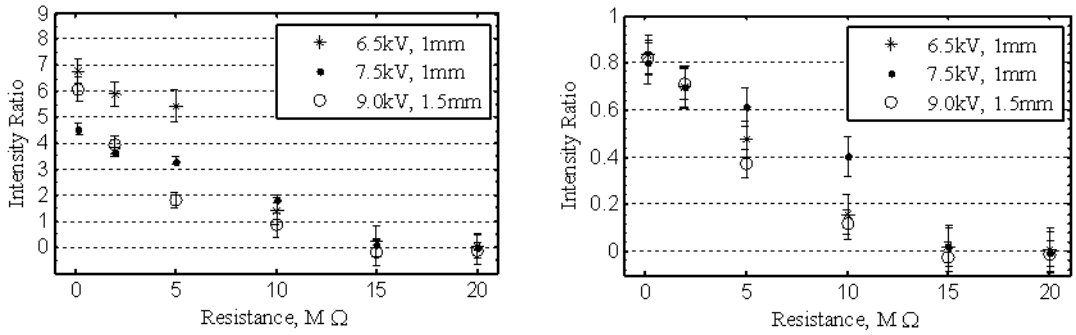

Figure 3.2. Light intensity as a function of resistance at 6.5kV, 7.5kV, and 9.0kV. Light intensity at the needle position (a) as a ratio to the light intensity of a mesh gap midpoint (no filament) and (b) as a ratio to a mesh node filament.

At 1 kOhm, the needle filament intensity is still less than the surrounding node filaments. Since the needle filament is surrounded by two other node filaments, it competes for surface charge with these nodes. If the needle filament was not surrounded by two other filaments we expect its ratio would rise to near 1 at 1 kΩ resistance. As the resistance increases, the filament eventually stops discharging. At this point the ratio of the needle filament to the non-discharging midpoint is zero since the background is subtracted from the needle value. Assuming there is no discharge in the mesh gap, this ratio signifies that no discharge occurs at the needle's position. The measured luminosity in the regions without filaments is due to ambient light. The camera's photos also have an inherent background light value that contributes to the intensity.

3.2. NEEDLE CURRENT AND VOLTAGE

Adjusting the needle self-biasing resistance affects the needle voltage and current. These results are shown in Figure 3.3. The voltage at the needle does not rise linearly as it begins to curve with increased resistance. Although the voltage appears as though it may approach a limit, the point of interest where the filament at the needle ceases to discharge is met before any definitive evidence of a limit. The voltage for the turn off of the filament at the needle is 476V and 560V respective to the driving voltages 6.5kV and

7.5kV. Both of these values correspond to 7% of the voltage across the DBD. The difference between the observed on and off state, 10MΩ to 15MΩ, is 108V and 119V.

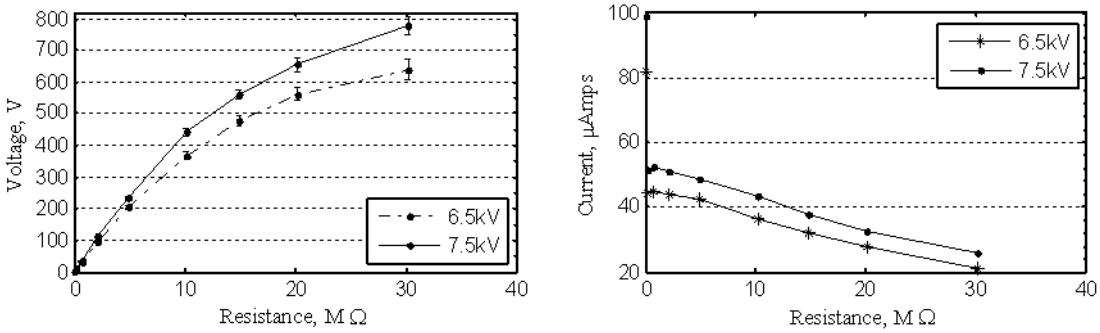

Figure 3.3. Voltage and current as a function of resistance at 6.5kV and 7.5kV. Changes to the needle's (a) voltage and (b) current due to changing resistors between the needle and ground.

The external voltage suppression caused by the biasing resistor at the 7.5 kV driving voltage is not large enough to bring the voltage difference across at the needle to the level of the 6.5 kV driving discharge. This implies that the intensity variation is not purely a result of reducing the voltage difference across the air gap, but rather preferential discharge at peak locations. In other words, more complex surface charge dynamics are responsible for these results.

The current through the needle is shown in Figure 3.3 (b). The current decreases linearly with the resistance. Although light intensity shows that there is no longer a filament forming at the needle, current continues to pass through the needle. This suggests that amount of charge allowed to displace on the surface is below a minimum value necessary for a filament to form. The current plot dips at 200kΩ and then spikes to 80microAmps at 1kΩ.

3.3. INCREASED FILAMENT INTENSITY

By reversing the set up – the needle lead wire is attached directly to the ground reference and a resistor is placed between the mesh and the ground – increasing resistance decreases the potential drop across the DBD. The preference for filament

discharge is switched to the needle. As the potential on the mesh increases, the larger potential drop across the air gap between the needle and driving electrode draws more charge from the surrounding surface. Figure 3.4 shows the resulting filament changes from reversing the self-biasing process.

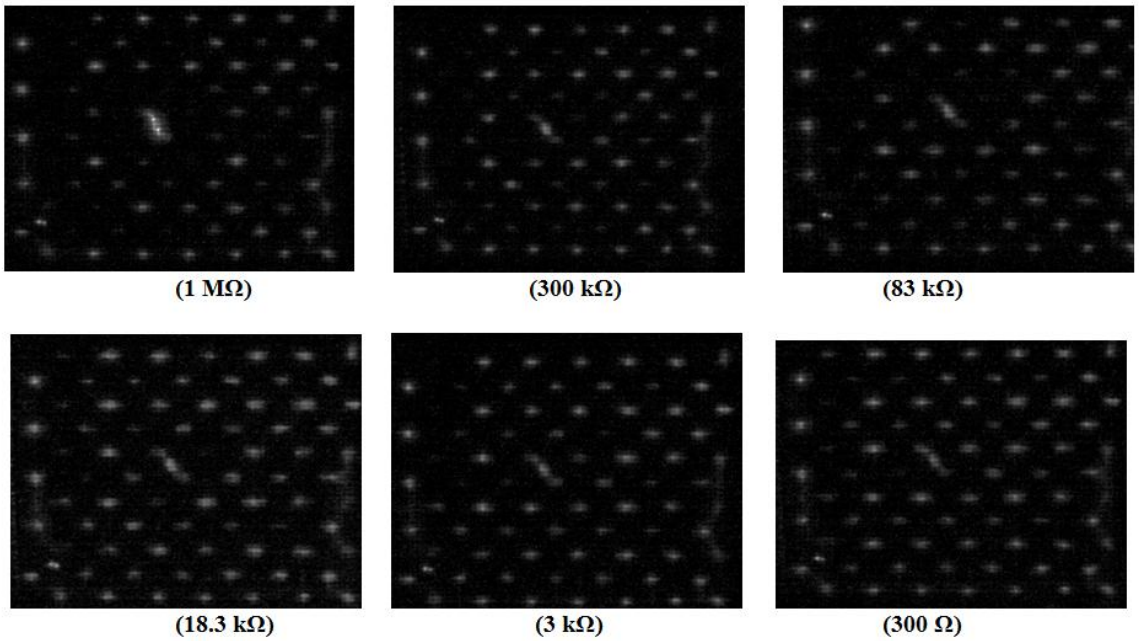

Figure 3.4. Photographs of the decreasing filaments surrounding the needle position. End on view of the dielectric surface operating at 6.5 kV with increasing resistances between the mesh electrode and ground reference. The surrounding filaments turn off while the needle filament intensity grows.

The reduction in the available surface charge decreases the intensity of the surrounding filaments until the mesh node filaments that are one mesh gap unit-distance away from the needle position have an intensity level less than double the mid-mesh (ambient) intensity. The two mesh nodes immediately adjacent to the filament also reduce in intensity. However, two high intensity points occur between the needle and these mesh nodes, at 1MΩ. Resistances beyond 1MΩ were not investigated since the current wave forms suggested a transition away from the preferred filament discharge to that of an arc between the needle and mesh electrodes, which might damage the set up.

Due to the interaction with more than 10 surrounding filaments, the intensity of the needle filament, shown in Figure 3.5, is significantly different than the self-biased

needle intensity results of Figure 3.1. The change observed with the self-biased mesh occurs over a logarithmic space where orders of magnitude resistance change are required to increase the intensity of the needle filament. The maximum voltage created by the 1MΩ resistance was measured as 470V and the light intensity was 178% of the unaffected mesh filaments.

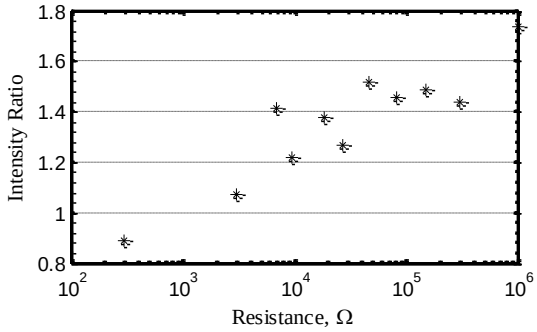

Figure 3.5. Light intensity as a function of resistance for a self-biased mesh. Light intensity at the needle position as a ratio to mesh filament intensity from unaffected areas of the DBD.

3.4. EFFECT OF RESIDUAL CHARGE

Charge build up on a DBD affects the charge transfer.[23] To analyze the effect of residual charge between consecutive data points, the charge was removed with acetone, the 9.0kV conditions were replicated, and compared with the previous data. The acetone was applied to a Kimwipe wrapped over a razor blade in order to fit into the air gap. Both dielectric surfaces were wiped with the Kimwipe prior to discharging. Acetone cleaned surfaces required breakdown voltage above that for non-acetone treated surfaces. To replicate the same DBD voltage value, the voltage was initially increased to 10kV to initiate breakdown then reduced back to 9kV.

The acetone treatment results in a higher needle light intensity level, as shown in Figure 3.6. Although elevated in magnitude, the trend of the acetone data follows that of the non-acetone treatment. The filament transitions from on to off between 10MΩ and 15MΩ for both cases. The difference in intensity ratio between the two cases, at the maximum intensity value (200kΩ), is 0.1 for the needle to mesh filament ratio (3.6b) and 1.6 for the needle to mesh gap ratio (3.6a).

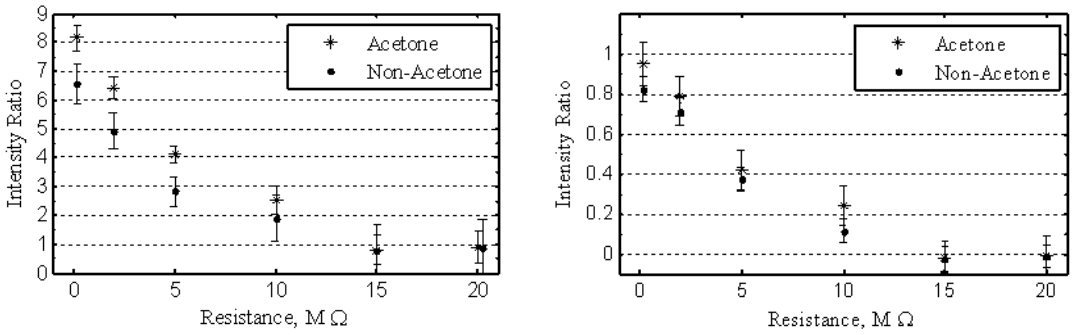

Figure 3.6. Light intensity of the acetone and non-acetone treatment as a function of resistance at 9.0kV. Light intensity at the needle position (a) as a ratio to the light intensity of a mesh gap midpoint and (b) as a ratio to a mesh node filament. Air gap distance set at 1.5mm.

The bias voltage increases only slightly with the acetone treatment and the trend of the non-acetone data closely follows it, as shown in Figure 3.7. The maximum voltage difference between the two sample sets occurs at 15MΩ and is 10.4V; a difference of 1.6%. With the consistency of voltage values and similar intensity trends, the effect of charge build up on the dielectric surface is negligible for this study considering the additional effect the acetone treatment has on the breakdown voltage.

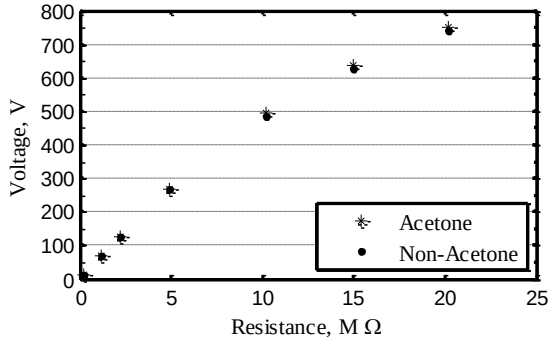

Figure 3.7. DBD voltage for the acetone and non-acetone treatment as a function of resistance at 9.0kV. Air gap distance set at 1.5mm.

4. ELECTRIC FIELD MODELING

The experimental DBD was simulated using Computer Simulations Technologies (CST), Electromagnetic Studios to determine the electric field formed over the needle and mesh filaments. Field transitions between 10MΩ and 15MΩ are associated with the light intensity transition from an on to off state. Excited charged particles in these fields are used to explain the observed light intensity variations. The potential distribution and electric fields produced by these simulations are analyzed to estimate light intensity of the filament at the needle relative to the filament at the mesh node. Since the discharge of the filament occurs over ~200ns,[45] the applied electric field, with a 312.5μs period, is considered constant during the discharge period. The focus of this modeling is on understanding how changes in the field affect the needle vs. mesh filament formation.

The applied electric field used in the simulation corresponds to the maximum voltage drop, i.e., the time when the driving voltage is at its maximum value. Since the applied voltage and voltage bias were measured by their peak values, the maximum voltage value was simulated. Since only the magnitudes of the fields will change between driving voltage conditions, a trend and ratio analysis can still be performed to find the relevant field conditions that affect the light intensity variation. Although the model assumes no free charge or time variation on the order of the discharge period (~200ns), the electrostatic results provide an understanding of the boundary conditions of the filaments.

The 3D model was created using the in-house CAD software. The wire mesh of the model, shown in Figure 4.1, replicates the height difference between the intertwining wires following a sinusoidal path along the horizontal and vertical orientation of the mesh weave. When placed against the surface of the dielectric, the wire closest to the surface creates the lowest potential drop. Additionally the model contains a cylindrical electrode placed within the mesh to simulate the needle electrode. The end of the cylinder is flush with the dielectric replicating the assembly of the physical needle and dielectric.

The electric field in the air gap was calculated using a low frequency, electrostatic solver. The potential boundary conditions consisted of a zero voltage applied to the mesh (cathode electrode), the maximum driving voltage applied to the external surface of the

1.0mm dielectric (anode electrode), and the measured needle voltage applied to the cylindrical needle electrode. The boundary conditions perpendicular to the dielectric surface were set to allow only tangential electric fields. The boundary behind the needle and mesh was set as an open boundary, 0.5 mm away from the solid model. The materials chosen for the simulation came from the CST library. Both dielectrics were made of lossy glass pyrex ($\varepsilon = 4.87$), the air gap ($\varepsilon = 1.00059$), and the conducting materials (needle and mesh) were made of perfect electrical conductors (PEC).

The finite element simulation mesh was also constructed using the CST software with tetrahedral unit shapes. The finite elements of the dielectrics, air gap, and conducting components all had a maximum dimension of 0.03 mm. Local refined mesh volumes had a maximum mesh size of 0.02 mm to create 50 simulation mesh nodes across the air gap and 30 nodes between the center points of the needle and mesh. These refined areas included: the 0.1 mm dielectric and an oval section inserted 0.1mm deep into the 1.0mm dielectric and extending across the air gap. The remaining model volume had a mesh size of 0.03 mm.

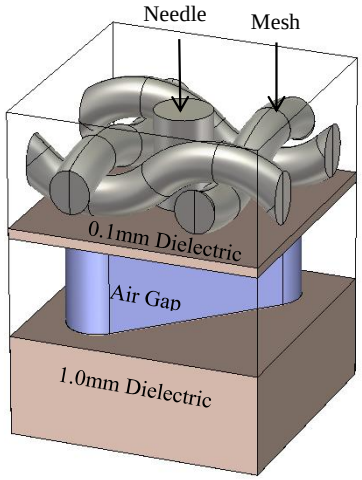

Figure 4.1. Isometric view of the 3D CST model. The oval volume in the Air Gap defines section of refined simulation mesh for the air gap, the remaining air gap volume is not shown for clarity.

5. RESULTS

The electrostatic solver calculated the potential distribution, the electric field, and the displacement field within the model volume. The results are presented below and are used in the remainder of this analysis to determine the aspect of the field that caused the observed intensity decrease and eventual extinction of the filament. It is important to remember that the experimental results showed the needle filament intensity decreasing as the self-biasing resistance increased and eventually turning extinguishing at the 15 MΩ case. Therefore analysis of the simulation data focuses on how the field changes as the self-biasing resistance approaches the 15MΩ case.

5.1. LONGITUDINAL ELECTRIC FIELD

The cross-section – defined by the center line of the needle filament and line that passes through both the needle and mesh center lines – of the longitudinal electric field (the field perpendicular to the dielectric surface) is plotted in Figure 5.1. These contour plots display the general form of the electric field when the needle filament is fully active (0.2MΩ), minimally active (10MΩ), and no longer visible (15MΩ). For conditions 0.2-10MΩ the longitudinal field along the centerline of the needle and away from the cathode is larger than the longitudinal field along the centerline of the mesh. The difference between needle and mesh fields ($\Delta E(x) = E(x)_{Needle} - E(x)_{Mesh}$) at all locations along the centerline is shown in Figure 5.2. The field near the cathode dielectric surface is 11% larger at the mesh than at the needle even when the needle is biased by 0.2 MΩ. This is due to the difference in the geometry of the needle and mesh. The mesh wire curvature creates a concentration in the field compared with the flat surface of the needle. At 15MΩ, the needle longitudinal field at the anode surface transitions to less than the field of the mesh. Then all points along the needle centerline are less than their respective counterparts along the mesh centerline. For clarity, the far end of the Figure 5.2(a) is expanded in Figure 5.2 (b). At the dielectric anode the curve of the 15MΩ approaches zero. Both needle and mesh apply the same amount of longitudinal force on a unit of charge at the dielectric anode for the filament extinction condition.

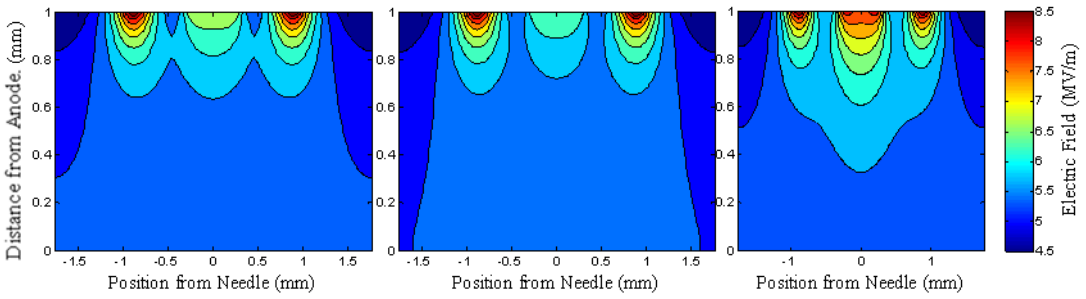

(15 MΩ) (10 MΩ) (0.2 MΩ)

Figure 5.1. Contour of longitudinal electric field. Three of the five needle bias conditions are presented: 15 MΩ, 10 MΩ, and 0.2 MΩ. The filament transition occurs between 15MΩ and 10MΩ.

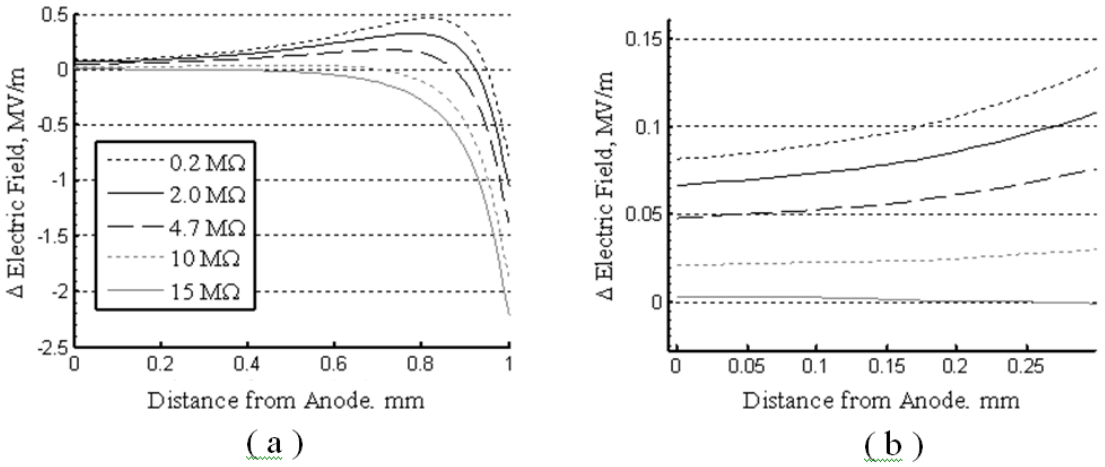

(a) (b)

Figure 5.2. Difference between needle and mesh centerline electric field**.** The electric field difference between the needle and mesh across the air gap (a) from the anode dielectric (z = 0mm) to the cathode dielectric (z = 1mm) and (b) an expansion of (z = 0mm to z = 0.3mm).

5.2. POTENTIAL

The difference between the potential along the centerline of the needle and the potential along the centerline of the mesh ($\Delta\phi(x) = \phi(x)_{Needle} - \phi(x)_{Mesh}$) is plotted in Figure 5.3 (a). For the extinction condition, the plot shows the needle at a higher potential than the mesh for all centerline positions. The expanded section in Figure 5.3 (b) shows the potential difference near the dielectric anode with a 1.5V difference on the anode dielectric surface. The lower energy state of the mesh centerline for each cross section

along the filament length means charge will flow perpendicularly from the needle filament to the mesh filament dependent upon the conductivity of the path.

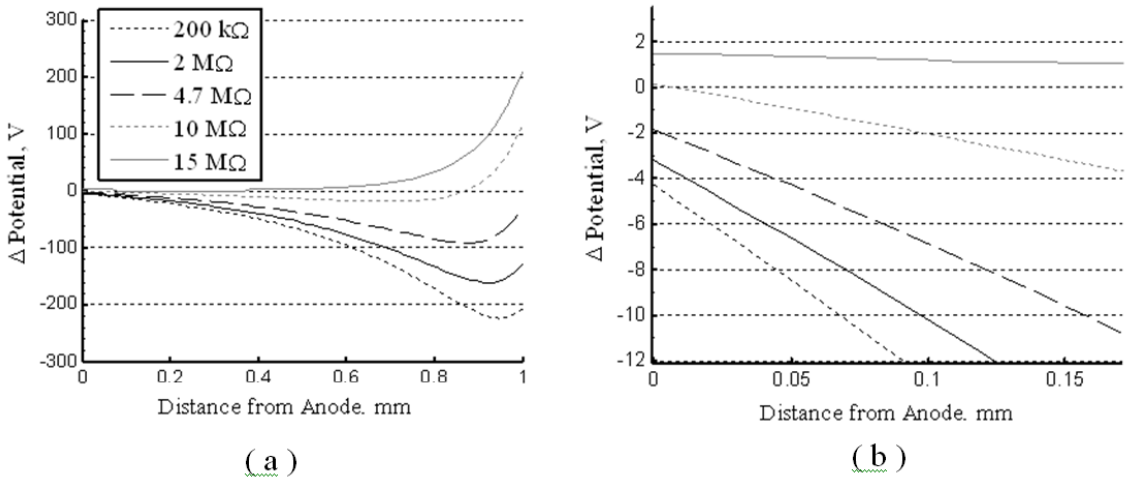

Figure 5.3. Difference between needle and mesh centerline potential. The voltage difference between the needle and mesh across the air gap (a) from the anode dielectric (z = 0mm) to the cathode dielectric (z = 1mm) and (b) an expansion of (z = 0mm to z = 0.2mm).

5.3. TRANSVERSE ELECTRIC FIELD

The transverse field (parallel to the dielectric surface), over the spatial cross-section of Figure 5.1, applies a force to free charges that moves them towards or away from the needle centerline. The transverse fields, positioned along the filament centerlines at the anode dielectric surface, the centerline midpoint, and the cathode dielectric surface for the 0.2-15MΩ conditions are shown in Figure 5.4. These plots illustrate the voltage bias dependent change of the electric force directed between the needle and mesh filaments. At the cathode dielectric surface, the needle and mesh charges are isolated by the transverse force directing mesh and needle positive charges towards their respective centerlines. At the cross-section of the centerline halfway point and near the anode dielectric surface (Figure 5.4, 0.5mm and 0.9mm), the needle and mesh charge is isolated by the transverse fields for conditions 0.2-10 MΩ. At the 15MΩ condition, the needle transverse field relaxes near the cathode and reverses near the

anode. The resulting force draws negative charge on the anode towards the needle filament position.

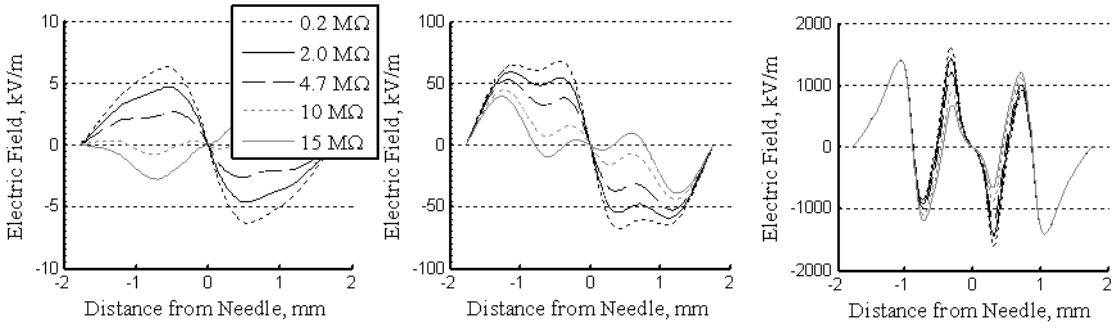

Figure 5.4. Transverse electric field as a function of x-position. The transverse electric field which intersects the needle and mesh node positions at different distances away from the anode dielectric for the range of bias conditions (0.2MΩ – 15MΩ).

The largest ratio of transverse field to longitudinal field for any point is 0.16 located at the cathode dielectric. Since the distance between the dielectrics (1.0 mm) is on the order of the distance between the needle and mesh position (0.88 mm), the movement of free charge in the gas volume is dominated by the 4.7-7.8 MV/m longitudinal field with relatively little transverse movement along the filament. The majority of lateral charge movement will occur on the charged dielectric surfaces where the longitudinal force is balanced by the dielectric normal force. The transverse force then dominates and has a compounding effect on the surface charge, which is present beyond the period of the filament discharge. Since the transverse fields isolate the needle and mesh charges present on the cathode dielectric surface, charge transfer between the needle and mesh filaments is assumed to occur on the anode dielectric surface.

5.4. FREE SURFACE CHARGE LIMITATION

The charge density on the dielectric surfaces was estimated by the displacement field, with units [C/m^2] from the simulation. The displacement field and an integral form of Gauss's Law, Equation 8, were used to compare the dielectric surface charge at the

needle with the surface charge at the mesh. At the interface of the two mediums, Gauss's Law can be simplified to Equation 9 [46] so that the difference between the normal components of the dielectric (D_d) and air (D_{air}) equal the surface charge (σ). The surface charge is assumed to build up during discharge on the dielectric until it reduces the electric field across the gas gap to below the dielectric strength of air ($E_b = 3\ MV/m$). Equation 10 is then used to determine the respective needle and mesh surface charge from the simulation data.

$$\oint_S \vec{D} \cdot \vec{n} da = \int_V \rho d^3 x \tag{8}$$

$$(\vec{D}_d - \vec{D}_{air}) \cdot \vec{n} = \sigma \tag{9}$$

$$D_d - \varepsilon_o \varepsilon_{air} E_{air} = \sigma \tag{10}$$

The surface charges on the cathode dielectric surface at the needle and mesh locations were estimated by taking the surface integrals. The areas of integration were selected by using the areas which fell within a minimum field value over the needle and mesh positions. The distribution of charge at 0.2MΩ is plotted in Figure 5.5 with the integration area for 0.2MΩ condition outlined. The ratios shown in Figure 5.6 of the needle to mesh charge vary by < 5% for different minimum field values selected with the condition that they do not eliminate or combine the needle and mesh areas. At the filament extinction condition the charge at the needle and mesh are equal.

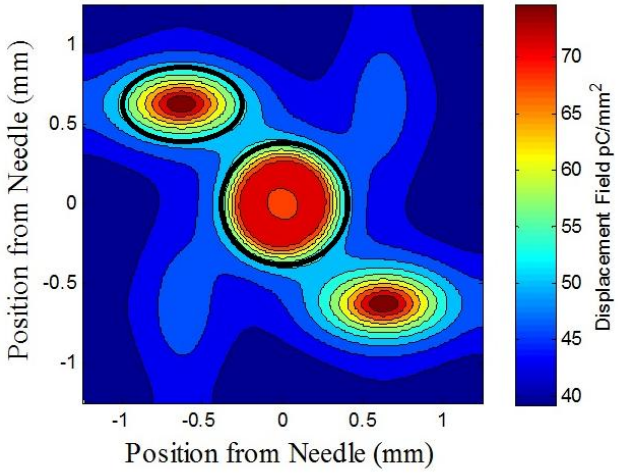

Figure 5.5. Contour map of the displacement field on the cathode dielectric surface, at 0.2MΩ. Representative of the distribution of the charge on the dielectric surface. The black outlines are the perimeter of the integration areas.

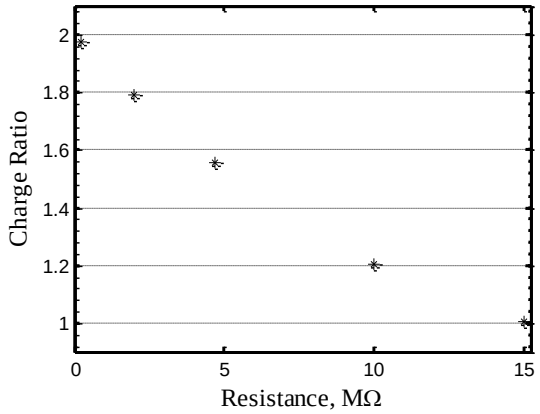

Figure 5.6. Ratio of needle to mesh charge, on the cathode dielectric. Charge calculated from the displacement field charge distribution.

The same analysis was not conducted on the anode dielectric since the charge distribution varies by 1% at the 0.2MΩ condition and <0.01% for the 15MΩ condition. Charge distributions on the anode dielectric surface are assumed to be independent of longitudinal field distribution and not inhibit transverse movement of surface charge.

6. DISCUSSION

In the context of the previously discussed filament formation physics, the field changes are used to explain the experimental results of the light intensity. At the 15MΩ condition, light intensity measurements give evidence that no filament forms at the needle position. The measured needle voltage biases of the 475V and 560V for the respective 6.5kV and 7.5kV driving voltages do not bring the electric field below the dielectric strength of air. The charge that would otherwise travel through the filament must be redistributed to offset the field forming along the centerline above the needle to prevent a filament from forming.

6.1. FILAMENT EXTINGUISHING MECHANISM

At the 15MΩ condition the potential at all positions along the mesh centerline is lower than the respective positions along the needle centerline. Considering the filament is highly conductive along its length, this puts the entire filament as a whole at a higher potential than the mesh filament. The transverse electric field on the cathode dielectric surface prevents the surface charge on the cathode from moving between filaments. The transverse electric field along the gas gap is < 16% of the longitudinal field and does not have time to significantly affect the charge distribution within the air gap. The transverse electric field on the anode transitions at the 15MΩ from positive to negative, reversing the current of surface charge. The uniformity of the charge density on the anode with variation of 1% - 0.01% create a uniform surface resistance. Charge transfer between the two filaments can only appreciably occur on the anode dielectric surface, the dielectric furthest from the needle electrode.

With constant surface resistance, surface current between the mesh and needle is related to the surface voltage difference between the two positions. For the 0.2MΩ – 4.7MΩ conditions, the potential difference ($\Delta\varphi = \varphi_{Needle} - \varphi_{Mesh}$), shown in Figure 6.1, is negative so that the current is directed towards the needle. This directs the electrons from the filament at the needle away from the needle position. Increased needle bias decreases the potential difference between the needle and the mesh position. This decreases the flow of electrons from the needle position to the mesh position on the

anode. At 10MΩ the potential difference is zero and no electrons travel from the needle position to the mesh position. At 15MΩ the current becomes negative. Positive charge moves away from the needle position on the anode dielectric and the electrons from the mesh position move towards the needle position. The surface charge transfer displaces the field along the needle centerline so that the gas breakdown does not occur.

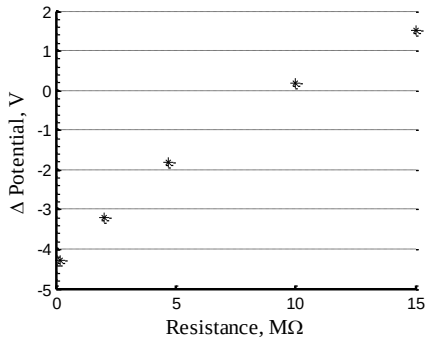

Figure 6.1. Potential difference between the needle and mesh on the anode dielectric surface. The potential difference is representative of the negative surface current (electron flow) directed from the mesh to the needle.

For the reversed polarity of the driving voltage, the electric field magnitude remains the same but the directions switches. The charge movement still occurs on the anode dielectric but with a reversed current direction. Surface electrons move away from the needle centerline towards the mesh centerline to transfer across the gas gap through one of the mesh filaments.

6.2. LIGHT INTENSITY RELATIONSHIP

The relationship between the modeled field values and measured light intensity originates from Equation 11,[47-49] the instantaneous light intensity flux rate (ψ) equal to the excitation flux rate (number of electron ionizations per cross-sectional area per time).

$$\psi(x,t) = \alpha(x,t) n_e(x,t) u_e(x,t) \tag{11}$$

Since the light of the discharge was recorded along the axis of the filament and over a time period (125 ms) far greater than the discharge cycle (~200ns), [45] the total light intensity is the time and space integral of the instantaneous light intensity, as expressed in Equation 12.

$$\overline{\psi} = \int_T \int_L \alpha(x,t)\, n_e(x,t)\, u_e(x,t)\, dx dt \tag{12}$$

The electric field oscillation has a period of 312.5μs so the applied electric field is assumed constant for the period of time when the filament is producing light. The electrons constitute the initial current charge carriers, when the majority of the current and light emission occurs in the first ~20ns.[47] The light intensity from a single discharge is approximated as an instantaneous delta function where the value for α is considered constant with respect to time and obtained from the initial discharge field values.

The electron number density and the drift velocity can be combined in the electron current density, as shown in Equation 13.

$$n_e u_e = \frac{J_e}{e} \tag{13}$$

The time integral of the current density results in the surface charge over the cross-section of the filament, Equation 14.

$$q_s = \int_T J_e(x,t) dt \tag{14}$$

The radius of the filament is dependent upon the applied voltage and pressure, so it is assumed constant across the gap as well as between the needle and the mesh filaments.[38] The surface charge is then just a constant in the line integral along the filament and represents the total electron charge (majority of the initial transferred charge) that passes across the filament. The ratio of the light intensities can then be simplified to Equation 15

where the filament cross-sectional area is the same for both needle and mesh so that the areas cancel. The light intensity flux areas also cancel since the same cross-section was used for intensity sampling.

$$\frac{\overline{\psi}_N}{\overline{\psi}_M} = \frac{q_N \int_L \alpha_N(x)dx}{q_M \int_L \alpha_M(x)dx} \tag{15}$$

The first Townsend coefficient is integrated over the length of the gap using Equation 16 to relate the coefficient to the electric field.

$$\alpha(x) = pAe^{\left(-\frac{Bp}{E}\right)} \tag{16}$$

The first Townsend coefficient (α) represents the number of ionzing electron-nuetral collisions per unit distance as a function of E / p, defined by the empirical Equation 16. The coefficient values A = 8.805 and B = 258.45, provided by a Sandia National Laboratories Report,[50] are curve-fits to a collection of literature data.

Due to the small variation between the electric fields, the ratios of the Townsend coefficient are 1 ± 0.002 for each voltage bias condition. The light intensity variation, for this approximation, is then solely dependent upon the total charge that crosses the air gap. The charge ratio is compared to the light intensity in Figure 6.2. Since there is no discharge at 15MΩ, the calculated surface charge is fixed to zero at 15MΩ while maintaining the charge trend by subtracting the 15MΩ ratio value ~ (1:1) from the total charge ratio. As justification, there will be a point at which a certain amount of charge exists at the surface of dielectric but no discharge occurs. For this case, that occurs at the 1:1 ratio where charge competition eliminates the needle filament.

The assumption is supported by the results of Figure 6.2, where the calculated trend of the light intensity falls along the average light intensity trends of the two adjacent mesh nodes for 6.5kV and 9.0kV. The light intensity of the 7.5kV has a 160%

offset from the calculated values at 10MΩ but its initial and final values converge with all sets of data. This trend may be due to additional surface charge built up across the dielectric surface over areas of the mesh wire close to the dielectric but not at the mesh node. The agreement of the calculated data and the cleaner filament data, at 6.5kV and 9.0kV, suggests that the trend of light intensity can be correlated with the electron charge transferred.

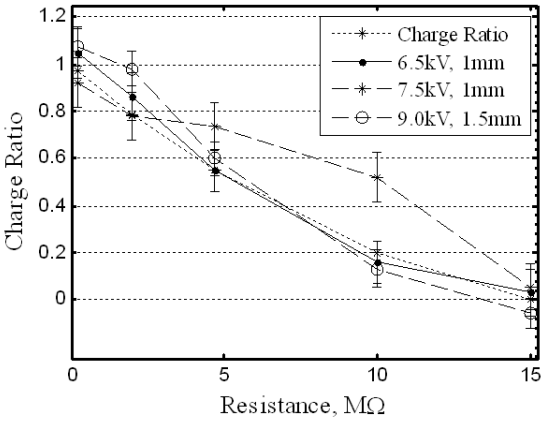

Figure 6.2. Calculated and measured light intensity as a function of resistance. The averaged light intensity values of the two adjacent filaments for 6.5kV, 7.5kV, and 9.0kV are compared to the simulation surface charge ratio of the needle filament to the adjacent filament. The calculated value assumes no intensity at 15MΩ, setting the trend of the total charge to zero.

7. CONCLUSION

The data presented demonstrates the capability of a voltage biased by a resistive load applied to an individual electrode to turn on and off a single filament while adjacent to other discharging filaments in a DBD. The light intensity of the filament ranges from ~100% to 0% of the surrounding filaments intensities. Peak voltages of 476V and 560V respective to the 6.5kV and 7.5kV driving voltages are required to completely turn off the filament. However, lesser voltage changes of 100V can cause the observed transition between a discharging filament and no filament. This relatively small change keeps the voltage difference applied across the gas gap above the breakdown voltage for air. The transition from discharge to no discharge at the needle is then dependent upon the space charge interaction between the needle filament and its adjacent filaments.

The reverse of the self-bias process was demonstrated by applying a resistive load to the mesh. The needle filament intensity doubled to 180% of the surrounding reference filament intensity for a 470V bias rise applied to the mesh. The increased current preference through the needle filament rerouted surrounding charge away from the mesh node filaments which reduced their intensity to less than twice the ambient intensity value.

The effect of built-up charge was investigated by comparing an acetone wiped dielectric surface to a non-acetone treated surface for discharging. The acetone treatment raised the required breakdown voltage and light intensity values. However, the light intensity trend of the acetone treatment was consistent with the non-acetone treatment and the filament transitioned to an off state between the same resistive values for both treatments. The largest difference in voltage values was 10.4V (1.6% of the needle bias voltage). The effect of cleaning the dielectric surface with acetone for each discharge was determined to be negligible for this study.

Simulations of the field conditions for the biased needle produced trends with the 15MΩ extinguishing condition. The filament turns off when: 1) the electric field of the needle is less than the field of the mesh at all respective points along the two filament centerlines, 2) the charge at the needle and the mesh on the cathode dielectric are equal, and 3) the transverse field between the needle and the mesh at the anode dielectric

creates a current from the needle to the mesh when the driving voltage polarity is positive and a current from the mesh to the needle when the driving voltage polarity is negative. These trends are associated with the movement and redistribution of charge particles, specifically electrons, on the anode dielectric surface. Charge transferred from the mesh filament displaces the field at the needle so that there is no breakdown at 15MΩ. Space charge and cathode surface charge both have transverse fields that don't allow translational charge movement. The variation of the light intensity is related to the total charge transferred across the air gap, represented by the surface charge at the needle. The light intensity trend agrees with the shifted surface charge trend.

Control of a DBD filament intensity has been demonstrated by changing an applied non-driving bias voltage by less than 7% of the driving voltage value, while the filament was adjacent to other fixed filament discharges. This investigation also showed that the voltage variation can affect other discharges beyond the immediately adjacent filaments. The interaction between these filaments is determined by the charge interaction on the dielectric with the uniform field distribution that allows charge to move between filament positions.

BIBLIOGRAPHY

[1] Dong, L., Xiao, H., Fan, W., Zhao, H., and Yue, H. "A Plasma Photonic Crystal With Tunable Lattice Constant," *IEEE Transactions on Plasma Science* Vol. 38, No. 9, 2010, pp. 2486-2490.doi: 10.1109/TPS.2010.2055586

[2] Dong, L. F., Fan, W. L., Wang, S., Ji, Y. F., Liu, Z. W., and Chen, Q. "Pattern formation in dielectric barrier discharges with different dielectric materials," *Physics of Plasmas* Vol. 18, No. 3, 2011, p. 033506.doi: 10.1063/1.3566003

[3] Wang, Y., Dong, L., Liu, W., He, Y., and Li, Y. "Generation of tunable plasma photonic crystals in meshed dielectric barrier discharge," *Physics of Plasmas* Vol. 21, No. 7, 2014, p. 073505.doi: 10.1063/1.4889900

[4] Fan, W., Zhang, X., and Dong, L. "Two-dimensional plasma photonic crystals in dielectric barrier discharge," *Physics of Plasmas* Vol. 17, No. 11, 2010, p. 113501.doi: 10.1063/1.3503625

[5] Dong, L., Li, B., Lu, N., Li, X., and Shen, Z. "Hexagonal superlattice pattern consisting of colliding filament pairs in a dielectric barrier discharge," *Physics of Plasmas* Vol. 19, No. 5, 2012, p. 052304.doi: 10.1063/1.4717466

[6] Sakaguchi, T., Sakai, O., and Tachibana, K. "Photonic bands in two-dimensional microplasma arrays. II. Band gaps observed in millimeter and subterahertz ranges," *Journal of Applied Physics* Vol. 101, No. 7, 2007, p. 073305. doi: 10.1063/1.2713940

[7] Sakai, O., Maeda, J., Shimomura, T., and Urabe, K. "Functional composites of plasmas and metamaterials: Flexible waveguides, and variable attenuators with controllable phase shifts)," *Physics of Plasmas* Vol. 20, No. 7, 2013, p. 073506.doi: 10.1063/1.4816698

[8] Sinclair, J., and Walhout, M. "Dielectric-Barrier Discharges in Two-Dimensional Lattice Potentials," *Physical Review Letters* Vol. 108, No. 3, 2012, p. 035005.URL: http://link.aps.org/doi/10.1103/PhysRevLett.108.035005

[9] Osamu, S., and Kunihide, T. "Plasmas as metamaterials: a review," *Plasma Sources Science and Technology* Vol. 21, No. 1, 2012, p. 013001.URL: http://stacks.iop.org/0963-0252/21/i=1/a=013001

[10] Pendry, J. B., Holden, A. J., Stewart, W. J., and Youngs, I. "Extremely Low Frequency Plasmons in Metallic Mesostructures," *Physical Review Letters* Vol. 76, No. 25, 1996, pp. 4773-4776. URL:http://link.aps.org/doi/10.1103/PhysRevLett.76.4773

[11] Pendry, J. B., Holden, A. J., Robbins, D. J., and Stewart, W. J. "Magnetism f conductors and enhanced nonlinear phenomena," *IEEE Transactions on Microwave Theory and Techniques* Vol. 47, No. 11, 1999, pp. 2075-2084.doi: 10.1109/22.798002

[12] Zhang, H.F., Liu, S.B., and Li, B.X. "Investigation on the properties of omnidirectional photonic band gaps in two-dimensional plasma photonic crystals," *Physics of Plasma* No. 23, 2016, p.012105.

[13] Marr, G. V. *Plasma spectroscopy*. Amsterdam, New York [etc.] :: Elsevier Pub. Co., 1968.

[14] Sakai, O., Shimomura, T., and Tachibana, K. "Negative refractive index designed in a periodic composite of lossy microplasmas and microresonators," *Physics of Plasmas* Vol. 17, No. 12, 2010, p. 123504.doi: 10.1063/1.3524561

[15] Naz, M., Ghaffar, A., Rehman, N., Shahid, S., and Shukrullah, S. "Characterization of an In-house Built 50 Hz Single Dielectric Barrier Discharge System Having Asymmetric Electrodes," *International Journal of Engineering & Technology IJET-IJENS* Vol. 12, No. 05, 2012, pp. 53-60.

[16] Oliveri, G., Werner, D. H., and Massa, A. "Reconfigurable Electromagnetics Through Metamaterials—A Review," *Proceedings of the IEEE* Vol. 103, No. 7, 2015, pp. 1034-1056.doi: 10.1109/JPROC.2015.2394292

[17] Benford, J., and Swegle, J. *High-Power Microwaves*: Artech House, 1992.

[18] Liu, C.-H., Neher, J. D., Booske, J. H., and Behdad, N. "Investigating the effective range of vacuum ultraviolet-mediated breakdown in high-power microwave metamaterials," *Journal of Applied Physics* Vol. 116, No. 14, 2014, p. 143302.doi: 10.1063/1.4897219

[19] Seviour, R., Tan, Y. S., and Hopper, A. "Effects of high power on microwave metamaterials," *Advanced Electromagnetic Materials in Microwaves and Optics (METAMATERIALS), 2014 8th International Congress on*. 2014, pp. 142-144.

[20] Chien-Hao, L., Neher, J. D., Booske, J. H., and Behdad, N. "Investigating the Physics of Simultaneous Breakdown Events in High-Power-Microwave (HPM) Metamaterials With Multiresonant Unit Cells and Discrete Nonlinear Responses," *IEEE Transactions on Plasma Science* Vol. 42, No. 5, 2014, pp. 1255-1264.doi: 10.1109/TPS.2014.2313873

[21] Schamiloglu, E. "High power microwave sources and applications," *Microwave Symposium Digest, 2004 IEEE MTT-S International*. Vol. 2, 2004, pp. 1001-1004 Vol.2.

[22] Manheimer, W. M., Fliflet, A. W., St. Germain, K., Linde, G. J., Cheung, W. Gregers-Hansen, V., Danly, B. G., and Ngo, M. T. "Initial cloud images with the NRL high power 94 GHz WARLOC radar," *Geophysical Research Letters* Vol. 30, No. 3, 2003, pp. 1-4.doi: 10.1029/2002GL016507

[23] Kogelschatz, U. "Dielectric-Barrier Discharges: Their History, Discharge Physics, and Industrial Applications," *Plasma Chemistry and Plasma Processing* Vol. 23, No. 1, 2003, pp. 1-46.doi: 10.1023/a:1022470901385

[24] Valentin, I. G., and Gerhard, J. P. "Dynamics of dielectric barrier discharges in different arrangements," *Plasma Sources Science and Technology* Vol. 21, No. 2, 2012, p. 024010.URL: http://stacks.iop.org/0963-0252/21/i=2/a=024010

[25] Dong, L., Shang, J., He, Y., Bai, Z., Liu, L., and Fan, W. "Collective vibration of discharge current filaments in a self-organized pattern within a dielectric barrier discharge," *Physical Review E* Vol. 85, No. 6, 2012, p. 066403.URL: http://link.aps.org/doi/10.1103/PhysRevE.85.066403

[26] Kogelschatz, U. "Filamentary, patterned, and diffuse barrier discharges," *IEEE Transactions on Plasma Science* Vol. 30, No. 4, 2002, pp. 1400-1408.doi: 10.1109/TPS.2002.804201

[27] Sakai, O., Sakaguchi, T., and Tachibana, K. "Photonic bands in two-dimensional microplasma arrays. I. Theoretical derivation of band structures of electromagnetic waves," *Journal of Applied Physics* Vol. 101, No. 7, 2007, p. 073304.doi: 10.1063/1.2713939

[28] Zhang, H.-F., Liu, S.-B., and Li, B.-X. "Investigation on the properties of omnidirectional photonic band gaps in two-dimensional plasma photonic crystals," *Physics of Plasmas* Vol. 23, No. 1, 2016, p. 012105.doi: 10.1063/1.4939540

[29] Zhang, H.-F., Ding, G.-W., Li, H.-M., and Liu, S.-B. "Complete photonic band gaps and tunable self-collimation in the two-dimensional plasma photonic crystals with a new structure," *Physics of Plasmas* Vol. 22, No. 2, 2015, p. 022105.doi: 10.1063/1.4906886

[30] Zhang, H.-F., Liu, S.-B., and Jiang, Y.-C. "Tunable all-angle negative refraction and photonic band gaps in two-dimensional plasma photonic crystals with square-like Archimedean lattices," *Physics of Plasmas* Vol. 21, No. 9, 2014, p. 092104.doi: 10.1063/1.4894213

[31] Park, W., and Wu, Q. "Negative effective permeability in metal cluster photonic crystal," *Solid State Communications* Vol. 146, No. 5–6, 2008, pp. 221-227.doi: 10.1016/j.ssc.2007.10.042

[32] Wu, Q., and Park, W. "Negative index materials based on metal nanoclusters " *Applied Physics Letters* Vol. 92, No. 15, 2008, p. 153114.doi: 10.1063/1.291

[33] Eliasson, B., and Kogelschatz, U. "Nonequilibrium volume plasma chemical processing," *IEEE Transactions on Plasma Science* Vol. 19, No. 6, 1991, pp. 1063-1077.doi: 10.1109/27.125031

[34] Lieberman, M. A. *Principles of plasma discharges and materials processing*. Hoboken, N.J. :: Wiley-Interscience, 2005.

[35] Itikawa, Y. "Cross Sections for Electron Collisions with Nitrogen Molecules," *Journal of Physical and Chemical Reference Data* Vol. 35, No. 1, 2006, pp. 31-53.doi: 10.1063/1.1937426

[36] Ryzko, H. "Drift velocity of electrons and ions in dry and humid air and in water vapour," *Proceedings of the Physical Society* Vol. 85, No. 6, 1965, p. 1283.URL: http://stacks.iop.org/0370-1328/85/i=6/a=327

[37] Gangwar, R. K., Levasseur, O., Naudé, N., Gherardi, N., Massines, F., Margot, J., and Stafford, L. "Determination of the electron temperature in plane-to-plane He dielectric barrier discharges at atmospheric pressure," *Plasma Sources Science and Technology* Vol. 25, No. 1, 2016, p. 015011.URL: http://stacks.iop.org/0963-0252/25/i=1/a=015011

[38] Eliasson, B., Egli, W., and Kogelschatz, U. "Modelling of dielectric barrier discharge chemistry," *Pure and Applied Chemistry* Vol. 66, No. 6, 1994, pp. 1275-1286.doi: 10.1351/pac199466061275

[39] Feng, Y., Ren, C. S., Nie, Q. Y., and Wang, D. Z. "Study on the Self-Organized Pattern in an Atmospheric Pressure Dielectric Barrier Discharge Plasma Jet," *IEEE Transactions on Plasma Science* Vol. 38, No. 5, 2010, pp. 1061-1065.doi: 10.1109/TPS.2010.2043121

[40] Loeb, L. B., and Meek, J. M. "The Mechanism of Spark Discharge in Air at Atmospheric Pressure. II," *Journal of Applied Physics* Vol. 11, No. 7, 1940, pp. 459-474.doi: 10.1063/1.1712796

[41] Meek, J. M., Craggs, J. D.,. "Electrical Breakdown of Gases," 1953.

[42] Emelyanov, O. A., and Shemet, M. V. "Single dielectric barrier discharge characteristics in needle-to-plane configuration," *Journal of Physics D: Applied Physics* Vol. 47, No. 31, 2014, p. 315201.URL: http://stacks.iop.org/0022-3727/47/i=31/a=315201

[43] Xinxin, W., Haiyun, L., Zhuo, L., Ting, M., and Ruili, M. "Influence of wire mesh electrodes on dielectric barrier discharge," *Plasma Sources Science and Technology* Vol. 15, No. 4, 2006, p. 845.URL: http://stacks.iop.org/0963-0252/15/i=4/a=030

[44] Qizheng, Y., Yunfei, W., Xingwang, L., Tian, C., and Guiwei, S. "Uniformity dielectric barrier discharges using mesh electrodes," *Plasma Sources Science and Technology* Vol. 21, No. 6, 2012, p. 065008.URL: http://stacks.iop.org/0963-0252/21/i=6/a=065008

[45] Kettlitz, M., Höft, H., Hoder, T., Reuter, S., Weltmann, K. D., and Brandenburg, R. "On the spatio-temporal development of pulsed barrier discharges: influence of duty cycle variation," *Journal of Physics D: Applied Physics* Vol. 45, No. 24, 2012, p. 245201.URL: http://stacks.iop.org/0022-3727/45/i=24/a=245201

[46] Jackson, J. D. *Classical electrodynamics*. New York, {NY}: Wiley, 1999.

[47] Morrow, R., and Lowke, J. J. "Streamer propagation in air," *Journal of Physics D: Applied Physics* Vol. 30, No. 4, 1997, p. 614.URL: http://stacks.iop.org/0022-3727/30/i=4/a=017

[48] Davies, A. J., Davies, C. S., and Evans, C. J. "Computer simulation of rapidly developing gaseous discharges," *Electrical Engineers, Proceedings of the Institution of* Vol. 118, No. 6, 1971, pp. 816-823.doi: 10.1049/piee.1971.0161

[49] Morrow, R. "Theory of negative corona in oxygen," *Physical Review A* Vol. 32, No. 3, 1985, pp. 1799-1809. URL:http://link.aps.org/doi/10.1103/PhysRevA.32.1799

[50] Warne, L., Jorgenson, R., Nicolaysen, S. "Ionization Coefficient Approach to Modeling Breakdown in Nonuniform Geometries," *Sandia National Laboratories* Vol. SAND2003-4078, 2003.

VITA

Matthew Crawford Paliwoda, attained his bachelor's degree in aeronautical and astronautical engineering from the University of Washington in 2012. There he participated in plasma undergraduate student research with the ZaP Flow Z-Pinch experiment. He then earned his master's degree in aerospace engineering from Missouri University of Science and Technology in July 2016, conducting graduate research with the Aerospace Plasma Laboratory.